# Triple Flame Structure and Dynamics at the Stabilization Point of a Lifted Jet Diffusion Flame



H.N. Najm*, R.B. Milne

Sandia National Laboratories

Livermore, CA 94551

and

K.D. Devine, and S.N. Kempka

Sandia National Laboratories

Albuquerque, NM 87185



Paper submitted to the $27^{th}$ International Symposium on Combustion.

University of Colorado, Boulder, CO.

August 2-7, 1998.

**Word Length**: Text: 3650, Figures: 1900, Equations: 140.

**Total:** 5690.

**Method:** unix word count.

**Presentation preference**: Oral presentation.

**Colloquium preference**: Turbulent premixed and partially premixed combustion.

* Corresponding Author, Sandia National Laboratories, P.O.Box 969, MS 9051, Livermore, CA 94551, USA. Tel/Fax: (510) 294-2054/2595, email: hnnajm@ca.sandia.gov

## DISCLAIMER

# Abstract

A coupled Lagrangian-Eulerian low-Mach-number numerical scheme is developed, using the vortex method for the momentum equations, and a finite difference approach with adaptive mesh refinment for the scalar conservation equations. The scheme is used to study the structure and dynamics of a forced lifted buoyant planar jet flame. Outer buoyant structures, driven by baroclinic vorticity generation, are observed. The flame base is found to stabilize in a region where flow velocities are sufficiently small to allow its existence. A triple flame is observed at the flame base, a result of premixing of fuel and oxidizer upstream of the ignition point. The structure and dynamics of the triple flame, and its modulation by jet vortex structures, are studied. The spatial extent of the triple flame is small, such that it fits wholly within the rounded flame base temperature field. The dilatation rate field outlines the edge of the hot fluid at the flame base. Neither the temperature field nor the dilatation rate field seem appropriate for experimental measurement of the triple flame in this flow.

## Introduction

Jet diffusion flames, involving a fuel jet surrounded with coflow air, have been studied both experimentally and numerically, with focus on the mechanism of lifted jet flame stabilization. The flame liftoff mechanism is of significance in turbulent jet flames because of its relevance to combustion stability. Liftoff theories abound in the literature and are discussed in recent studies [1,2]. Experimental studies in lifted jet flames have provided mean and instantaneous measurements of velocity and scalar fields, and flame liftoff heights [3,4,5,6,7].

The observed flow and scalar field structure in the vicinity of the stabilization point has suggested the existence of a triple flame at that location [8,9]. A triple flame is a particular flame structure observed under partially premixed flow conditions with gradients of mixture fraction [10,11]. Triple flames have not been observed experimentally in lifted jet flows. Their existence at the lifted flame base is suggested by the expected premixing of fuel and coflow air in going from the jet exit to the flame base. The structure of a triple flame at the base of the lifted flame would involve a diffusion flame branch which extends downstream from the stabilization point, and rich and lean premixed flame branches extending into the fuel and coflow streams respectively. Triple flames have been observed in numerical simulations of diffusion flames in flows with mixture fraction gradients, but not in lifted jet flames (perhaps because of poor spatial resolution). On the other hand, locally refined mesh computations of steady bunsen flames have shown evidence of a triple flame at the flame base [12].

In this study, we use a low Mach number reacting flow formulation with a coupled Lagrangian-Eulerian numerical scheme to study the stabilization of a lifted planar buoyant jet diffusion flame. Baroclinically generated outer buoyant vortex structures are observed, resulting in large modulation of the flame. We also observe a triple flame at the flame base, and study its structure and dynamics as it is modulated by jet vortex structures. The spatial extent of the triple flame in the present flow is small, such that it fits wholly within the rounded flame base temperature field. The computed dilatation rate field outlines the edge of the hot fluid at the flame base. Results suggest that neither the temperature field nor the dilatation rate field seem appropriate for experimental measurement of the triple flame in this flow.

## Model Formulation

We model the reacting jet flow using the low Mach number approximation [13], in a two-dimensional (2D) flow model. Since the domain of interest is open, the spatially uniform stagnation pressure $p_o$ is also constant in time.

The model implicitly utilizes the continuity equation, $\partial\rho/\partial t = -\nabla\cdot(\rho\mathbf{v})$, where $\mathbf{v} = (u, v)$ is the velocity vector, and $\rho$ is the density. The energy equation is developed using binary diffusion coefficients. We neglect radiation and Soret-Dufour effects, giving:

$$\frac{\partial T}{\partial t} = -\mathbf{v}\cdot\nabla T + \frac{1}{RePr}\frac{\nabla\cdot(\lambda\nabla T)}{\rho c_p} + \frac{1}{ReSc}\frac{\mathbf{Z}\cdot\nabla T}{c_p} + Da\frac{w_T}{\rho c_p} \tag{1}$$

where, $T$ is temperature, $\lambda$ is the thermal conductivity, $c_p$ is the specific heat at constant pressure, $Re$, $Pr$, $Sc$ are the Reynolds, Prandtl, and Schmidt numbers respectively. Further, $w_T = -\sum_{i=1}^{N} h_i w_i$ is the heat release source term, and $\mathbf{Z} = \sum_{i=1}^{N} c_{p,i} D_{iN} \nabla Y_i$, where $h_i$, $w_i$, $c_{p,i}$, $Y_i$ are the enthalpy, chemical production rate, specific heat, and mass fraction of species $i$ respectively, and, $D_{iN}$ is the binary mass diffusion coefficient of species $i$ into the $N$-th species, assumed dominant. For computational efficiency, mixture transport properties $(\mu(T), \lambda(T))$ are set to those of the dominant species.

We also write the state equation, $p_o = \rho T/\overline{W}$, where $\overline{W}$ is the effective molar mass of the mixture given by, $\overline{W} = 1/\sum_{i=1}^{N} Y_i/W_i$. And, for species $i$, using the assumption of dominant $N$-th species, the species conservation equation is found to be:

$$\frac{\partial Y_i}{\partial t} = -\mathbf{v}\cdot\nabla Y_i + \frac{1}{ReSc}\frac{\nabla\cdot(\rho D_{iN}\nabla Y_i)}{\rho} + Da\,\frac{w_i}{\rho} \tag{2}$$

where $Da$ is the Damköhler number. The chemical production rate, $w_i$, is generally given by the sum of contributions of elementary reactions with Arrhenius rates including forward and backward rates, third-body efficiencies, and pressure dependence [14]. The present results are based on a single-step global irreversible reaction as indicated below.

We discuss next the vorticity transport equation, and formulate the baroclinic and expansion field source terms necessary for the coupling between the Eulerian and Lagrangian schemes. The low Mach number vector momentum equation is :

$$\frac{D\mathbf{v}}{Dt} = -\frac{\nabla p}{\rho} + \frac{1}{Re}\frac{\mathbf{\Phi}}{\rho} + \frac{1}{Fr}\mathbf{g} \tag{3}$$

where, $\mathbf{\Phi} = \partial \tau_{ji}/\partial x_j$ is the divergence of the stress tensor, $p$ is the dynamic pressure, $\mathbf{g}$ is the gravitational acceleration, and $Fr$ is the Froude number.

Taking the curl of the momentum equation gives the vorticity ($\omega$) transport equation,

$$\frac{D\omega}{Dt} = -\omega(\nabla \cdot \mathbf{v}) + \frac{1}{\rho}\nabla\rho \times (\frac{1}{Fr}\mathbf{g} - \frac{D\mathbf{v}}{Dt}) + \frac{1}{Re}\frac{\nabla \times \mathbf{\Phi}}{\rho} \tag{4}$$

Then, for a patch of fluid of area $A$, taking the area integral of the vorticity equation gives the rate of change of circulation $\Gamma_A$ :

$$\frac{d}{dt}\int_A \omega \cdot dA = \frac{d\Gamma_A}{dt} = \int_A \left[\frac{1}{\rho}\nabla\rho \times (\frac{1}{Fr}\mathbf{g} - \frac{D\mathbf{v}}{Dt}) + \frac{1}{Re}\frac{\nabla \times \mathbf{\Phi}}{\rho}\right] dA \tag{5}$$

Note that the expansion term does not contribute to the change in circulation. The two remaining terms are the baroclinic and diffusion source terms, which are computed on the Eulerian mesh and provide the strengths of the local circulation source terms for the Lagrangian field.

We next evaluate the velocity divergence, using the continuity and state equations, with $dp_o/dt = 0$, giving :

$$\nabla \cdot \mathbf{v} = \frac{1}{T}\frac{DT}{Dt} + \overline{W}\sum_{i=1}^{N}\frac{1}{W_i}\frac{DY_i}{Dt}. \tag{6}$$

The terms on the right are computed on the Eulerian mesh, and their sum $\nabla \cdot \mathbf{v}$ becomes the local expansion source strength for the Lagrangian scheme, Eq. (4).

## Numerical Scheme

The numerical scheme uses a coupled combination of an Eulerian finite difference solution of the scalar conservation equations and the Lagrangian vortex method for the momentum equations [15]. The Eulerian solution uses Adaptive Mesh Refinement (AMR) [16] to allow efficient computation over a large range of length scales. The vortex method is inherently adaptive. This combination leads to an efficient overall scheme.

The energy and species equations are discretized on the multi-layered adaptive mesh. Diffusive terms are discretized using centered second-order differences. Convective terms are discretized using a second-order Godunov upwind scheme [17], resulting in a convective scheme that is stable for any grid Peclet number. Spatial discretizations are based on a rectangular uniform mesh, with special cell buffers around mesh edges to allow uniform-mesh derivative discretizations at those locations.

The vorticity transport equation is discretized using the Lagrangian vortex method [18]. We use second-order gaussian core functions, and ensure sufficient overlap between neighboring elements [19]. Redistribution of the vortex element field is implemented at a specified time-step interval to maintain accuracy [20,21]. Vortex elements are created from the initial condition, and subsequently at the jet inlet and in regions of non-zero baroclinic and diffusion source terms, based on Eq. (5). Using the Helmholtz decomposition [22], the velocity field is expressed as the sum of vortical, potential, and dilatational components, corresponding respectively to the contributions of vortex elements, domain boundaries, and expansion sources. The potential flow solution required to impose boundary conditions is computed using the Boundary Element Method [23]. An adaptive Fast Multipole Method [24] is used to compute velocities induced by vortex and boundary elements as well as expansion sources. The velocity field is computed at the centers of vortex elements, to be used in advecting them, and at the Eulerian mesh cell walls, to be used in the convection of scalars and the computation of baroclinic and diffusion source terms. Boundary conditions include inflow at the bottom boundary, slip vertical walls, and an outflow top edge.

A coupled Lagrangian-Eulerian time integration approach is constructed based on a second-order Runge-Kutta (RK2) predictor-corrector formulation for both the Lagrangian and Eulerian integrations. The RK2 procedure on the adaptive mesh is recursive, and uses

finer time steps on finer meshes so as to maintain numerical stability. The overall solution proceeds with global Lagrangian time steps, within which are imbedded Eulerian sub-steps. The integration procedure at each time step involves :

1. **Predictor:** Vortex elements are advected, using explicit first-order Euler time integration, with the local velocity. New elements are injected both at the domain inlet and from internal source terms. Scalar fields are integrated on all meshes using explicit Euler first-order time integration.
2. **Corrector:** Vortex elements are advected using second-order Runge-Kutta time integration based on the average of old and predicted velocity fields. Corrected circulation source terms are used to add circulation to existing elements and/or inject new elements, in addition to the corrected injection of elements at the domain inlet. Scalar fields are integrated using second-order Runge-Kutta time integration.

## Results

We consider a rectangular domain, 40 cm wide and 20 cm high, with a planar jet of fuel, of width 1.16 cm, centered on the domain centerline, at $x = 20$ cm, flowing vertically upward. The fuel jet velocity is 0.8 m/s, and is surrounded by coflow air with a 0.1 m/s velocity. The jet flow is forced with an impulse function at a frequency of 7.5 Hz, with a 50% forcing amplitude. This large amplitude forcing is purposely used to generate strong vortex structures in the vicinity of the flame base, less than one jet-width downstream of the inlet plane.

The composition of the fuel jet is 40% $CH_4$, 60% $N_2$ by volume. Both jet and coflow are at room temperature. We use a single-step irreversible global chemical mechanism : $CH_4 + 2O_2 \Rightarrow CO_2 + 2H_2O$, with forward rate $k_f = Ae^{-E/RT}$, where $A = 5.0\text{x}10^{22}$ (mole-cm-sec-K) and $E = 47600$ cal/mole. A comparison between a 1D opposed-jet diffusion flame solution [14,25], at a strain-rate of 17 $s^{-1}$, using this mechanism and a 46-step $C_1$ mechanism [26], is shown in Figure 1, suggesting that the flame model computed with the above mechanism is adequate. The flowfield is initialized with these global 1D profiles, which are arranged in 2D to correspond to two diffusion flames extending from the vicinity of the jet edges to the top of the domain. A global Lagrangian-Eulerian time step of 0.25 ms is used. Five levels of adaptive mesh refinement are used. The coarsest mesh, Mesh-0, is 64x32.

As the flow evolves in time, the adaptive mesh structure changes accordingly to maintain adequate spatial resolution. An example mesh structure is shown in Figure 2, for a fraction of the computational domain including half the jet extent in $x$, corresponding to a 4x4 cm region at the jet exit. Mesh levels 0-5 are evident, with the finest mesh (Mesh-5) region corresponding to the steep shear layer at the jet exit and the base of the lifted flame. The region of Mesh-5 refinement narrows with downstream distance because the diffusion flame burning rate and profile gradients decay with downstream distance.

The jet flame structure is shown in Figure 3 at time 350 ms. The rounded base of the flame at the liftoff height is evident, and is similar to experimentally observed flame base results [7,3]. The flame base resides on the coflow side of the jet shear layers, where flow velocities are relatively low. The figure shows a pair of internal jet strucutures that were shed from the nozzle at an earlier time. Counter-rotating baroclinic vorticity is observed in the wake of these structures.

Outer baroclinic buoyant structures are also observed in Fig. 3, both at early and late stages of development. The corresponding Strouhal and Froude numbers, based on the jet width and the velocity difference between the jet and coflow, fall on the experimental fit observed in [27] for a large number of jet flame experiments.

A triple flame is observed at the flame base region, as shown in Figure 4, where the time evolution of the flame base and vorticity field is illustrated. In the first frame, the flow is relatively quiescent, prior to the forcing velocity pulse. The flame base/triple flame exists where the flow velocity is low enough to allow its survival. The heat release rate peaks at the triple flame tip, with a value six times that in the diffusion flame immediately downstream of it. Extending sideways from the flame tip are two partially premixed flame branches, a rich branch into the fuel stream and a lean branch into the coflow air. The spatial extent of the triple flame structure is small, as the three branches fit within the rounded flame base observed in the temperature field shown in Fig. 3. The rich branch is elongated with the faster jet fluid, and is generally longer than the lean branch. In the second frame, strong vorticity is observed emanating from the jet exit, as the forced jet velocity is increased. In the third frame, two distinct jet vortex structures are formed, and proceed to entrain the triple flame, moving it towards the jet centerline. The rich branch is virtually decimated as a result of the large flow velocities and strain-rates imposed by the vortices. The flame base is observed to curve inward behind the vortices. This motion continues and is accentuated in the fourth frame as the two vortices pass by the flame base. The triple flame structure is clearly stretched at this point, as both rich and lean branches are separated from the diffusion flame. The following frame shows the flame tip returning to its earlier location as the vortices move downstream. The rich triple flame branch is severely stretched by the jet vortices, and extends into the jet. As the vortices move further downstream, the flame base relaxes, as seen in the last frame, pointing downward and settling into the coflow side of the jet. The effect of the vortices continues to be felt by the diffusion flame as they flow downstream, as evidenced by the local peak in heat release rate moving downstream along the diffusion flame.

The mixture conditions at the triple flame can be further studied using the mixture fraction $Z = (1/2)[1 + (\nu_{oxidizer}/\nu_{fuel})X_{fuel} - X_{oxidizer}]$, where $\nu$ is the stoichiometric coefficient in the reaction mechanism, and $X$ is the mole fraction. At stoichiometric conditions $Z = 0.5$

irrespective of the dilution of the mixture.

The mixture fraction contours and the heat release rate at time 310 ms are shown superposed in Figure 5. The stoichiometric mixture fraction line ($Z = 0.5$) is seen to extend from the jet edge through the premixed stoichiometric front of the triple flame and along the diffusion flame. Also evident is the contortion of the $Z$-lines induced by the passage of the vortex pair, and the associated modification of the triple flame structure. This data suggests that the branches of the triple flame extend roughly by $\pm 10\%$ of the $Z$-range on either side of the stoichiometric line. Close inspection of the mixture fraction contour lines reveals a spreading of the lines on either side of the stoichiometric line in going from the jet exit plane to the flame base. This is an indication of premixing of jet and coflow fluids such that a premixed charge of $CH_4$ and $O_2$ is available at the triple flame. This premixing has been suggested in earlier experimental studies [3,4,28].

As noted in Najm *et al.* [29], $\nabla \cdot \mathbf{v}$ in a premixed flame is found to be dominated by reaction and heat diffusion, i.e. the first two terms in:

$$\nabla \cdot \mathbf{v} = Da \frac{w_T}{\rho c_p T} + \frac{1}{RePr} \frac{\nabla \cdot (\lambda \nabla T)}{\rho c_p T} + \frac{1}{ReSc} \frac{\mathbf{Z} \cdot \nabla T}{c_p T} - \frac{1}{\overline{W}} \frac{D\overline{W}}{Dt} \tag{7}$$

The same result holds for the premixed flame in the triple flame observed here. The $\nabla \cdot \mathbf{v}$ field is found to delineate the edge of the rounded temperature field at the flame base, with a peak immediately ahead of the triple flame, consistent with that region being a preheat zone. However, the results suggest that $\nabla \cdot \mathbf{v}$ does not exhibit a triple branch structure at the flame base, and hence would not be a useful indicator of the presence of a triple flame. Moreover, flow unsteadiness can lead to large changes in the heat diffusion term as observed in [29], casting doubt on the correlation of peak $\nabla \cdot \mathbf{v}$ with heat release.

The $\nabla \cdot \mathbf{v}$ field and its components are shown plotted along the stoichiometric $Z$-contour in Figure 6, at time 250 ms, along with the temperature field. The diffusion term is clearly responsible for the rise in $\nabla \cdot \mathbf{v}$ in the low temperature region of the flame, consistent with [29]. The lower plot illustrates the variation of tangential velocity, $\mathbf{v}_t$, and normal strain-rate, $\tau$, along the stoichiometric line. Thus $\mathbf{v}_t$ is normal to, and $\tau$ is tangential to, the triple flame at the flame base. The shape of the velocity profile is in agreement with earlier work [3,8]. The laminar burning speed computed with Chemkin [14,30] using the present global mechanism and triple flame mixture conditions is found to be $S_L = 10\,\mathrm{cm/s}$. The difference from the

expected value of 40 cm/s is because this mechanism was chosen to give acceptable diffusion flame profiles rather than premixed flame speed. The minimum velocity ahead of the triple flame in the figure is observed to be 13 cm/s. The difference from the 1D $S_L$ may be due to the assumption of binary diffusion into $N_2$, as well as flame base unsteadiness, the curvature of the triple flame, and the lateral fluxes corresponding to the triple flame structure. The range of time-variation of the observed velocity minimum over a forcing cycle is $[-4, 3]S_L$. Muñiz and Mungal [3] observed a [0,3]$S_L$ range in a turbulent lifted flame. The disagreement at the lower limit may be related to the relative strength of the organized 2D vortices in the present flow. Finally, the strain-rate is seen to rise to a peak of $90\,s^{-1}$ at the triple flame. The magnitude of this peak oscillates in time over the range [50,200] $s^{-1}$.

The peaks of $\nabla\cdot\mathbf{v}$ and its heat release and diffusion components in the triple flame region are shown plotted over four forcing cycles in Figure 7. This data indicates that the peaks of $\nabla\cdot\mathbf{v}$ are correlated with maxima in the peak diffusion term and minima in peak heat release rate. This inverse relationship of dilatation rate with flame heat release rate under unsteady flow is consistent with earlier work [29]. As seen in Fig. 6, the peak of $\nabla\cdot\mathbf{v}$ is primarily due to the diffusion term, which explains this strong correlation between them. The diffusion term maxima and heat release minima occur at time instants when the triple flame is exposed to strong tangential stretch rate due to the vortex flow field, as in Fig. 5, where the tangential strain-rate at the triple flame peaks at about $200\,s^{-1}$.

## Conclusions

A coupled Lagrangian-Eulerian numerical scheme was developed and used to model lifted buoyant jet flame dynamics. Global jet dynamics are consistent with experimental data, involving baroclinic vorticity generation and the evolution of large outer buoyant structures.

A triple flame was observed at the flame base, and its structure and dynamics were investigated. The spatial extent of the triple flame is small, such that it is imbedded within the rounded flame base temperature field. The flame base dynamics involve strong curvature and entrainement by passing vortices, consistent with experimental observations [7,3]. The triple flame branches are observed to fluctuate due to passing vortices as observed in [9].

The dilatation rate field is observed to delineate the edge of the rounded flame base, and does not exhibit a three-branch structure. It seems that neither temperature nor flow dilatation rate imaging would reveal the triple flame branches. A more direct measurement of heat release rate, such as imaging of HCO [29], may be necessary.

Flame stabilization in this flow is found to involve premixing and heating of the fuel and oxidizer streams ahead of the triple flame. The flame base resides where flow velocities are sufficiently small to allow its existence. Further studies with different flow and flame conditions, and with realistic chemical kinetics, are necessary to extend and establish the range of validity of these results.

## Acknowledgments

This work was supported by the US Deptartment of Energy (DOE), Laboratory Directed Research and Development (LDRD) program at Sandia National Laboratories (SNL), and by the DOE Office of Basic Energy Sciences, Chemical Sciences Division. HNN acknowledges the help of W.T. Ashurst SNL-CA in the formulation of the model problem and numerical setup.

## References


[1] Pitts, W.M., *Twenty-Second Symposium (International) on Combustion*, The Combustion Institute, 1988, , pp. 809–816.

[2] Takahashi, F., and Schmoll, W.J., *Twenty-third Symposium (International) on Combustion*, The Combustion Institute, 1990, , pp. 677–683.

[3] Muñiz, L., and Mungal, M.G., *Combustion and Flame*, 111:16–31 (1997).

[4] Schefer, R.W., Namazian, M., and Kelly, J., *Twenty-Second Symposium (International) on Combustion*, The Combustion Institute, 1988, , pp. 833–842.

[5] Clemens, N.T., and Paul, P.H., *Combustion and Flame*, 102:271–284 (1995).

[6] Everest, D.A., Driscoll, J.F., Dahm, W.J.A., and Feikema, D.A., *Combustion and Flame*, 101:58–68 (1995).

[7] Mueller, C.J., and Schefer, R.W., *WSS/CI97S-028* (1997) Spring Technical Meeting, The Western States Section of The Combustion Institute, April 14-15, Sandia National Laboratories, Livermore, CA.

[8] Ruetsch, G.R., Vervisch, L., and Liñan, T., *Phsics of Fluids*, 7(6):1447 (1995).

[9] Veynante, D., Vervisch, L., Poinsot, T., Linñan, T., and Ruetsch, G., *Center for Turbulence Research, Proceedings of the Summer Program*, Stanford, CA, (1994), Stanford University, Stanford Univ., , pp. 55–73.

[10] Dold, J.W., *Combustion and Flame*, 76:71 (1989).

[11] Echekki, T., and Chen, J.H., *Combustion and Flame* (1997) in press.

[12] Smooke, M.D., Ern, A., Tanoff, M.A., Valdati, B.A., Mohammed, R.K., Marran, D.F., and Long, M.B., *Twenty-sixth Symposium (International) on Combustion*, The Combustion Institute, 1996, , pp. 2161–2170.

[13] Majda, A., and Sethian, J., *Combustion Science and Technology*, 42:185–205 (1985).

[14] Kee, R.J., Rupley, F.M., and Miller, J.A., Sandia Report SAND89-8009B, Sandia National Labs., Livermore, CA., (1993).

[15] Najm, H.N., Schefer, R.W., Milne, R.B., Mueller, C.J., Devine, K.D., and Kempka, S.N., Technical report, Sandia National Laboratories, Albuquerque, New Mexico, (1997) in press.

[16] Devine, K., and Flaherty, J., *Appl. Numer. Math.*, 20:367–386 (1996).

[17] Bell, J.B., and Colella, P., *J. Comp. Phys.*, 85:257–283 (1989).

[18] Chorin, A.J., *J. Fluid Mech.*, 57(4):785–796 (1972).

[19] Anderson, C.R., *J. Comp. Phys.*, 61:417–444 (1985).

[20] Koumoutsakos, P.D., Phd thesis, Graduate Aeronautical Laboratories, California Institute of Technology, Pasadena, CA, (1993).

[21] Winckelmans, G.S., Salmon, J.K., Warren, M.S., Leonard, A., and Jodoin, B., *Second International Workshop on Vortex Flows and Related Numerical Methods*, Montréal, Canada, (1995).

[22] Najm, H.N., and Ghoniem, A.F., *Combustion Science and Technology*, 94:259–278 (1993).

[23] Kempka, S.N., Glass, M.W., Peery, J.S., and Strickland, J.H., Technical Report SAND96-0583, Sandia National Laboratories, Albuquerque, NM, (1996).

[24] Carrier, J., Greengard, L., and Rokhlin, V., *SIAM J. Sci Stat. Comput.*, 9:669–686 (1988).

[25] Lutz, A.E., Kee, R.J., Grcar, J.F., and Rupley, F.M., Sandia Report SAND96-8243, Sandia National Laboratories, Albuquerque, New Mexico, (1996).

[26] Smooke, M.D., Puri, I.K., and Seshadri, K., *Twenty-First Symposium (International) on Combustion*, Pittsburgh, PA, (1986), The Combustion Institute, , pp. 1783–1792.

[27] Hamins, A., Yang, J.C., and Kashiwagi, T., *Twenty-Fourth Symposium (International) on Combustion*, The Combustion Institute, 1992, , pp. 1695–1702.

[28] Everest, D., Feikema, D., and Driscoll, J.F., *Twenty-Sixth Symposium (International) on Combustion*, The Combustion Institute, 1996, , pp. 129–136.

[29] Najm, H.N., Paul, P.H., Mueller, C.J., and Wyckoff, P.S., *Combustion and Flame* (1997) in press.

[30] Kee, R.J., Grcar, J.F., Smooke, M.D., and Miller, J.A., Sandia Report SAND85-8240, Sandia National Labs., Livermore, CA., (1993).

## Figure Captions

**Figure 1.** Comparison between computed opposed jet diffusion flame solutions with a detailed $C_1$ mechanism and the present global mechanism.

**Figure 2.** A 4x4 cm region of the domain starting at the jet exit centerline ($x = 20, y = 0$), showing the adaptive mesh at a time 300 ms (third frame in Fig. 4). The jet edge is at 20.58 cm.

**Figure 3.** Overall jet flame structure shown using a color map for temperature (blue to red, 300-2000 K), and solid/dashed contours for positive/negative vorticity, at time 350 ms. Positive vorticity is counter-clockwise. Frame shows full domain height and 40% of the domain width.

**Figure 4.** Time evolution of the triple flame region from time 280 to 330 ms, starting at the top left hand frame and proceeding from left to right. Frames are 5x4.38 cm, extending to the domain edge at $y = 0$, and are 10 ms apart. The color map illustrates vorticity and contours indicate heat release rate.

**Figure 5.** The triple flame region at time 310 ms (fourth frame in Fig. 4). The color map illustrates heat release rate $w_T$ and contours indicate mixture fraction $Z$. Adjacent $Z$-contours are separated by 10% of the overall $Z$-range. The middle contour line on each side of the jet is the stoichiometric contour line, $Z = 0.5$.

**Figure 6.** Variation of various flow quantities along the stoichiometric mixture fraction line, extending from the jet edge at the inlet plane into the flame base and diffusion flame beyond. Data is at time 250 ms, and is shown for a length of 1.2 cm along the line.

**Figure 7.** A plot of the peak values of $\nabla \cdot \mathbf{v}$, $w_T/\rho c_p T$, and $\nabla \cdot (\lambda \nabla T)/\rho c_p T$ in the triple flame region, over a time span encompassing four forcing cycles.

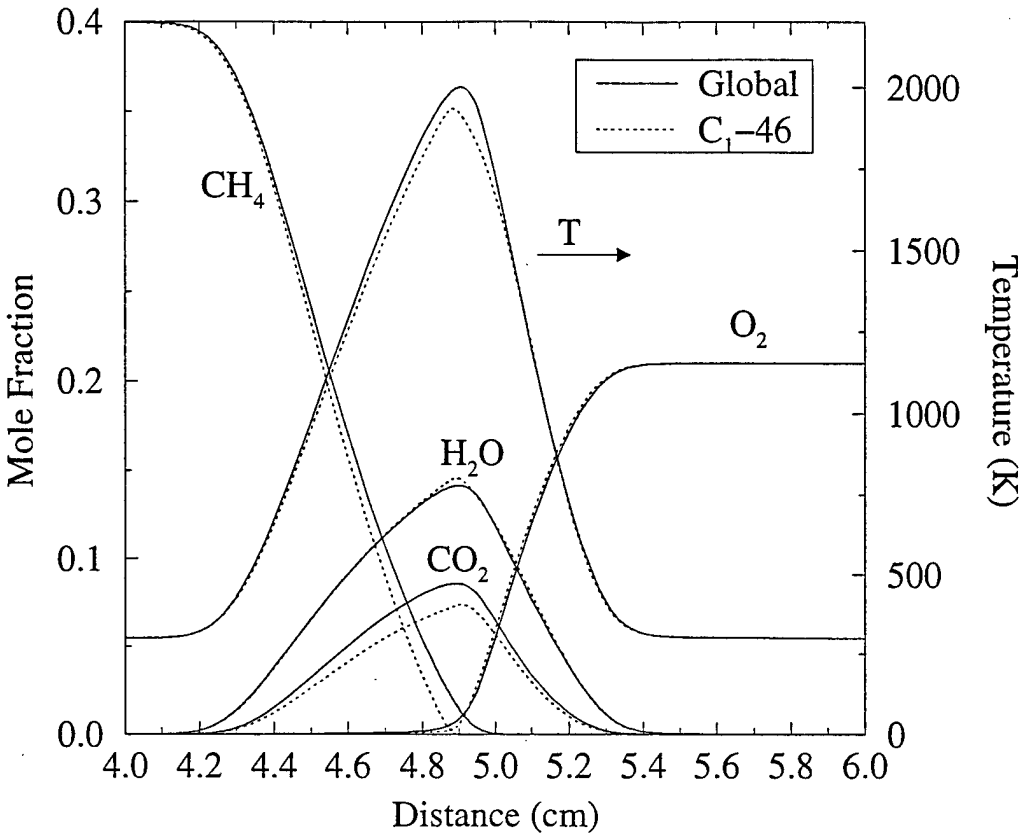


**Figure 1.** Comparison between computed opposed jet diffusion flame solutions with a detailed $C_1$ mechanism and the present global mechanism.

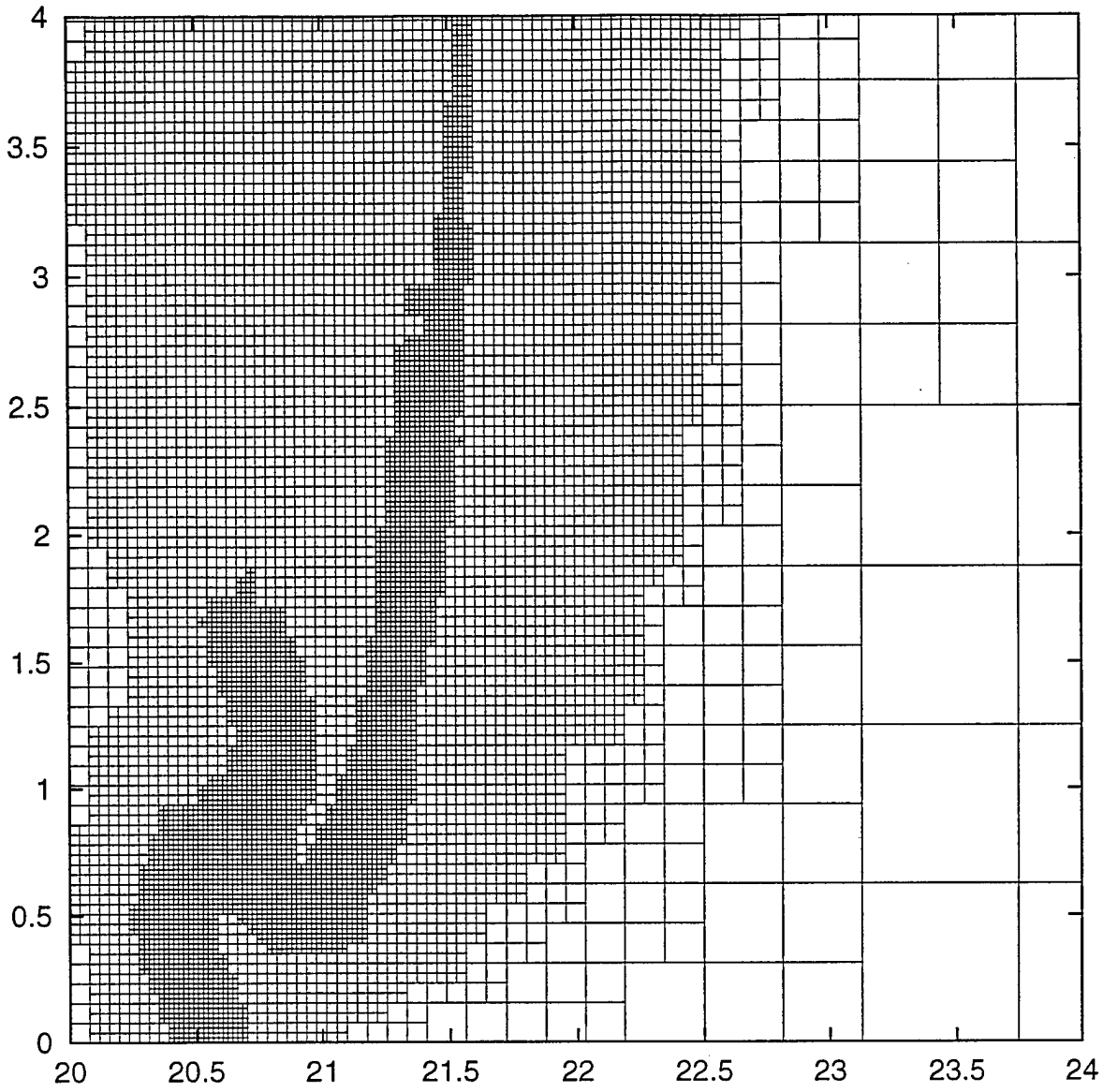


**Figure 2.** A 4x4 cm region of the domain starting at the jet exit centerline ($x = 20, y = 0$), showing the adaptive mesh at a time 300 ms (third frame in Fig. 4). The jet edge is at 20.58 cm.

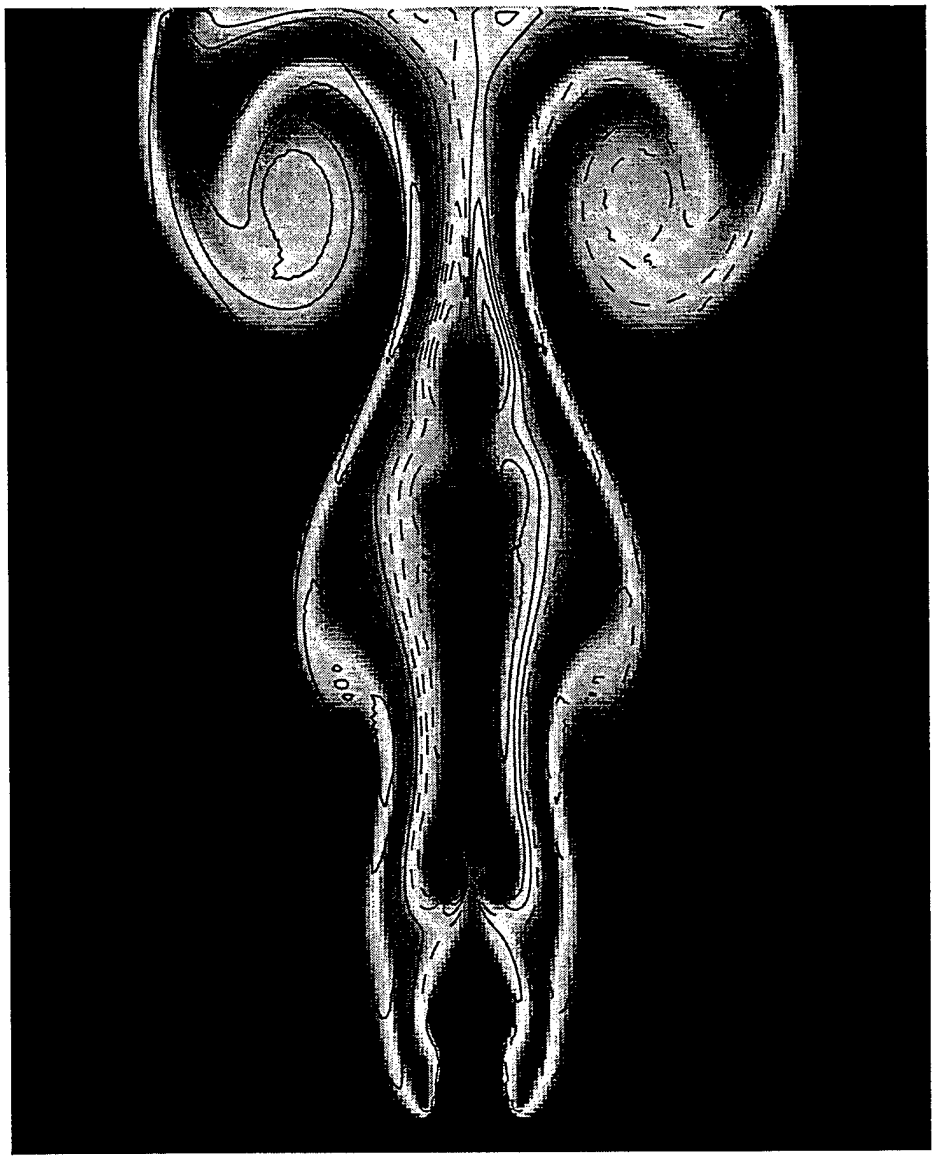

**Figure 3.** Overall jet flame structure shown using a color map for temperature (blue to red, 300-2000 K), and solid/dashed contours for positive/negative vorticity, at time 350 ms. Positive vorticity is counter-clockwise. Frame shows full domain height and 40% of the domain width.

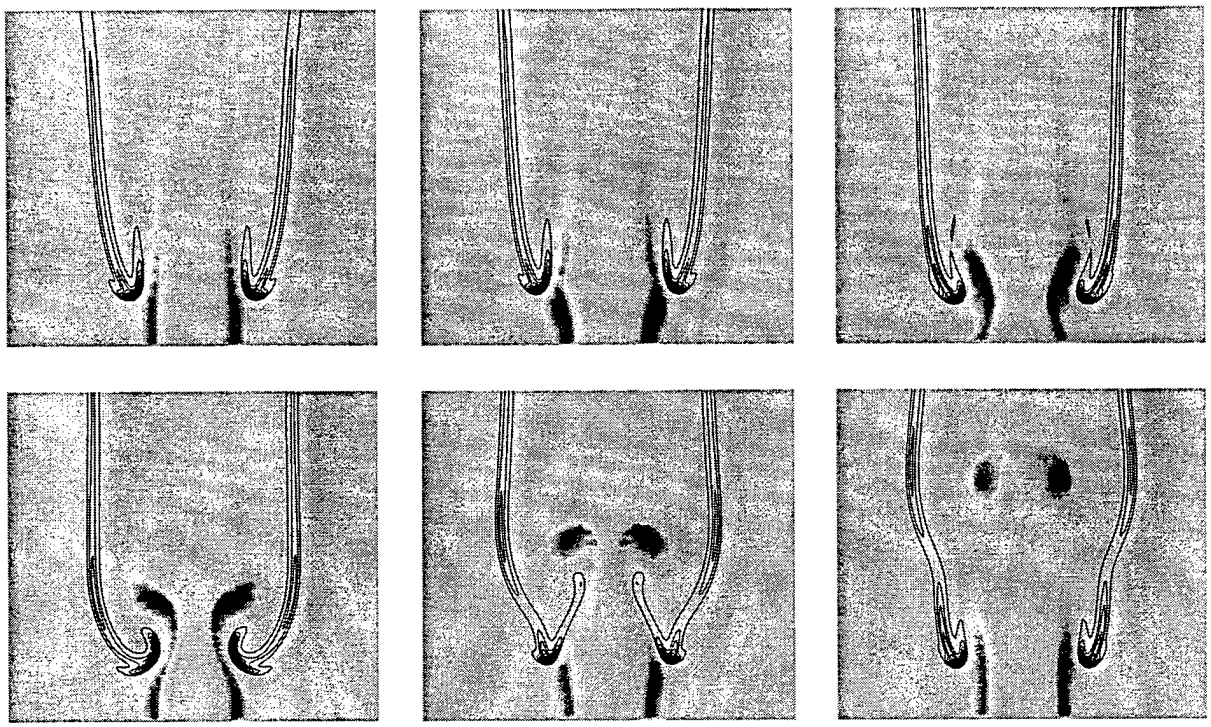

**Figure 4.** Time evolution of the triple flame region from time 280 to 330 ms, starting at the top left hand frame and proceeding from left to right. Frames are 5x4.38 cm, extending to the domain edge at $y = 0$, and are 10 ms apart. The color map illustrates vorticity and contours indicate heat release rate.

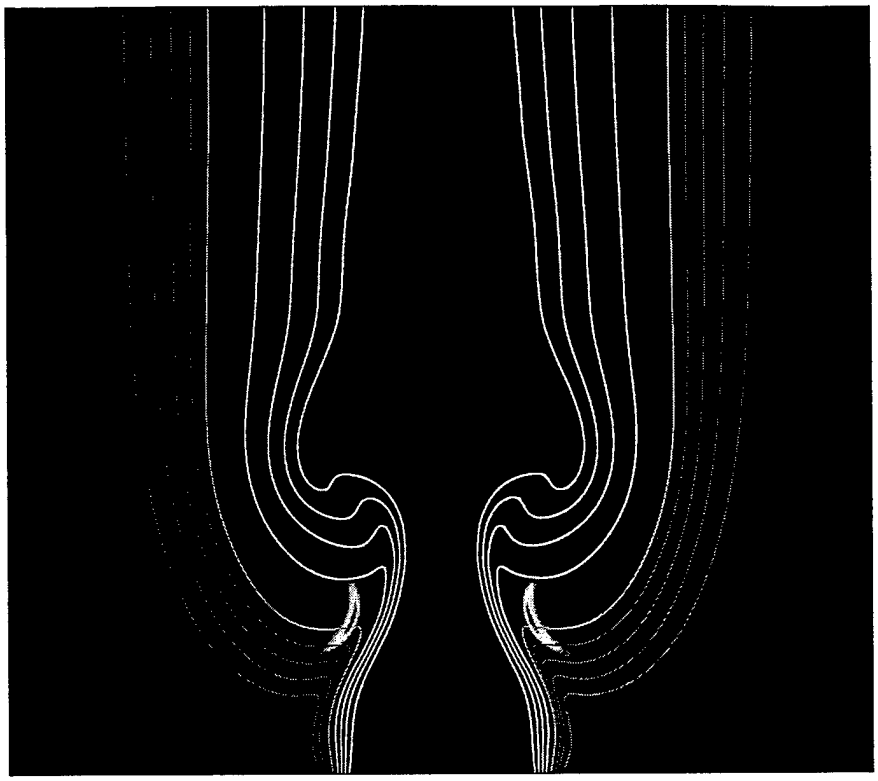

**Figure 5.** The triple flame region at time 310 ms (fourth frame in Fig. 4). The color map illustrates heat release rate $w_T$ and contours indicate mixture fraction $Z$. Adjacent $Z$-contours are separated by 10% of the overall $Z$-range. The middle contour line on each side of the jet is the stoichiometric contour line, $Z = 0.5$.

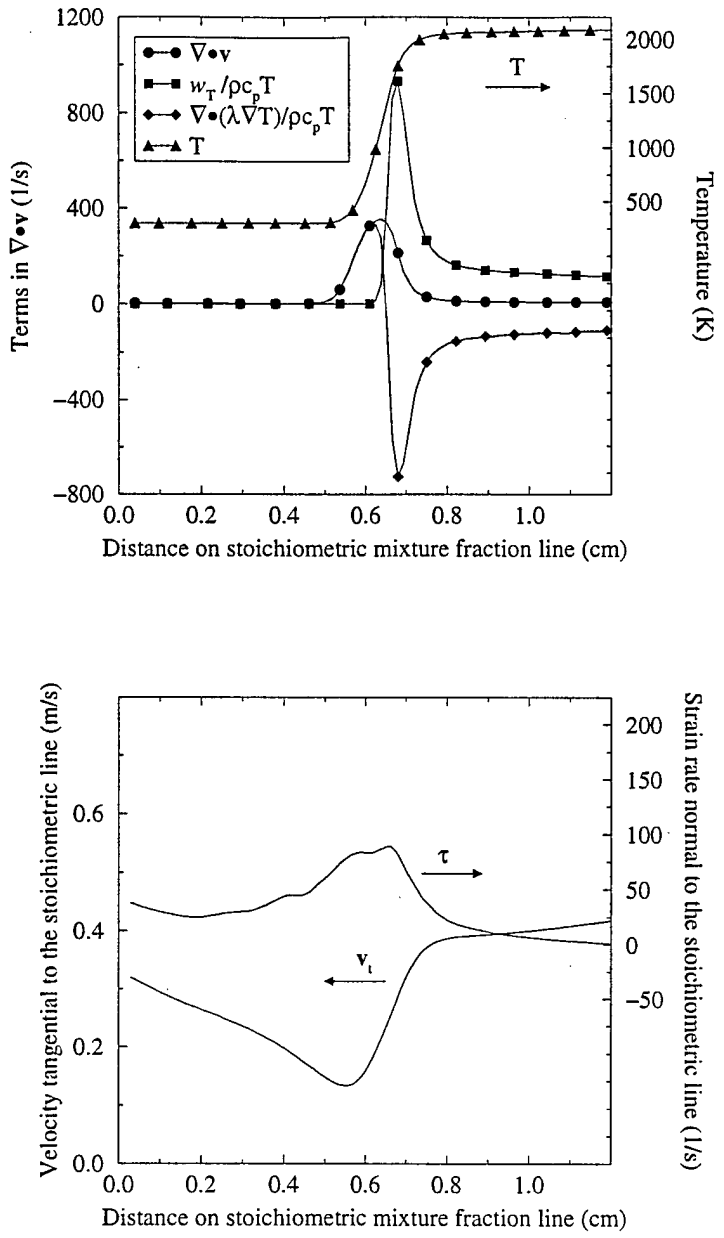


**Figure 6.** Variation of various flow quantities along the stoichiometric mixture fraction line, extending from the jet edge at the inlet plane into the flame base and diffusion flame beyond. Data is at time 250 ms, and is shown for a length of 1.2 cm along the line.

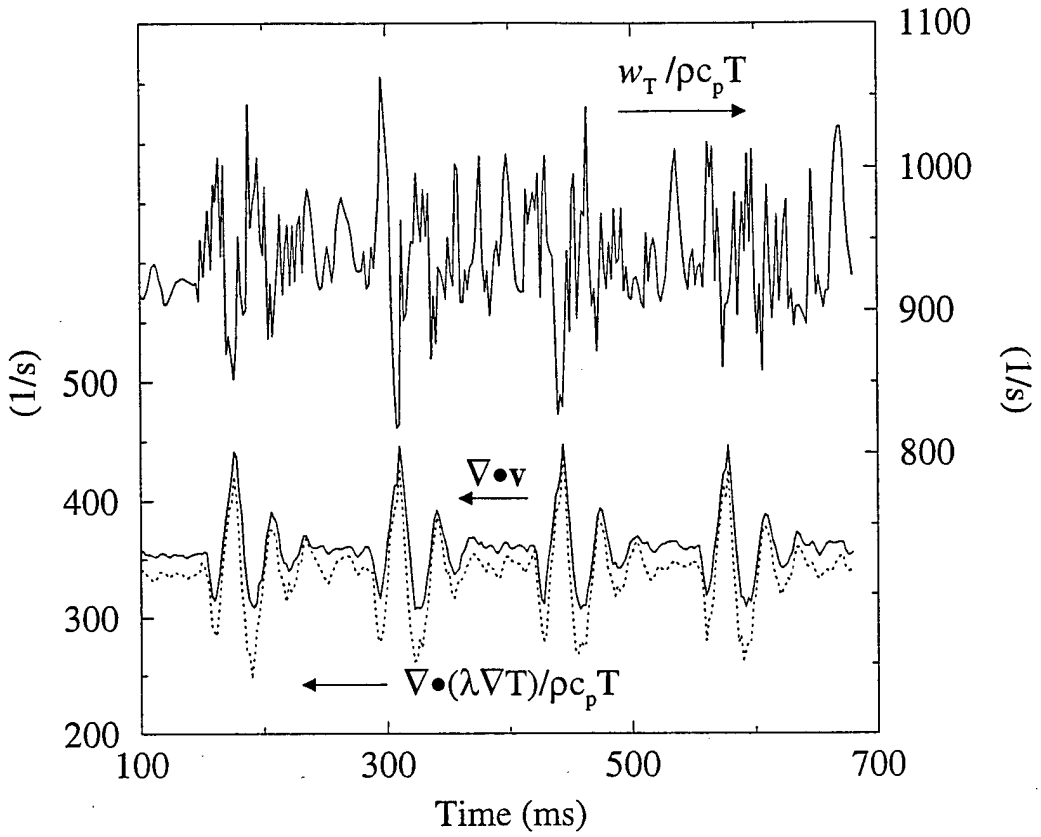


**Figure 7.** A plot of the peak values of $\nabla \cdot \mathbf{v}$, $w_T/\rho c_p T$, and $\nabla \cdot (\lambda \nabla T)/\rho c_p T$ in the triple flame region, over a time span encompassing four forcing cycles.

Report Number (14) SAND--98-8464C
CONF-980804--

Publ. Date (11) 199808
Sponsor Code (18) DOE/AO, XF
UC Category (19) UC-1409, DOE/ER



DOE